

# Fabricating functional circuits on 3D freeform surfaces via intense pulsed light-induced zinc mass transfer

Ning Yi <sup>1,†</sup>, Yuyan Gao <sup>2,†</sup>, Antonino Lo Verso Jr <sup>2</sup>, Jia Zhu <sup>2</sup>, Daniel Erdely <sup>2</sup>, Cuili Xue <sup>2,3</sup>, Robert Lavelle <sup>1</sup>, Huanyu Cheng <sup>1,2,\*</sup>

Deployment of functional circuits on a 3D freeform surface is of significant interest to wearable devices on curvilinear skin/tissue surfaces or smart Internet-of-Things with sensors on 3D objects. Here we present a new fabrication strategy that can directly print functional circuits either transient or long-lasting onto freeform surfaces by intense pulsed light-induced mass transfer of zinc nanoparticles (Zn NPs). The intense pulsed light can locally raise the temperature of Zn NPs to cause evaporation. Lamination of a kirigami-patterned soft semi-transparent polymer film with Zn NPs conforming to a 3D surface results in condensation of Zn NPs to form conductive yet degradable Zn patterns onto a 3D freeform surface for constructing transient electronics. Immersing the Zn patterns into a copper sulfate or silver nitrate solution can further convert the transient device to a long-lasting device with copper or silver. Functional circuits with integrated sensors and a wireless communication component on 3D glass beakers and seashells with complex surface geometries demonstrate the viability of this manufacturing strategy.

Keywords: Intense pulsed light; Zinc mass transport; 3D freeform surfaces; Functional circuits

#### Introduction

Currently, most electronic devices are fabricated by vacuum-based integrated circuit processes [1], screen printing [2], or additive manufacturing methods [3], all of which require a planar substrate for patterning functional materials. Because a convex or concave surface is not compatible with lithographic processes and traditional printers, the technique of transfer printing has been explored for heterogeneous integration of the thin film electronics onto curvilinear structures [4]. In addition to the complicated fabrication processes, the electronics also need to

be flexible and moldable to ensure robust performance over the shape transformation.

To achieve direct fabrication of electronic circuits on an arbitrary shape, advanced printing techniques have been developed, including omnidirectional printing [5], aerosol jet printing [6], and adaptive 3D printing [7]. However, disadvantages still exist for these direct writing methods. Omnidirectional printing relies on the precise motion control of the printing head and a perfect match between the target surface and the printing path [5]. Therefore, it is only achieved for a known regular surface, because the printing quality can be affected if there is a mismatch between the actual surface and the moving path of the printing head. High-resolution scanning of the target surface is necessary for other arbitrary surfaces. The design of ink formula-

<sup>&</sup>lt;sup>1</sup> Department of Materials Science and Engineering, The Pennsylvania State University, University Park, PA 16802, USA

<sup>&</sup>lt;sup>2</sup> Department of Engineering Science and Mechanics, Materials Research Institute, The Pennsylvania State University, University Park, PA 16802, USA

<sup>&</sup>lt;sup>3</sup> Institute of Nano Biomedicine and Engineering, Department of Instrument Science & Engineering, School of Electronic Information and Electrical Engineering, Shanghai Jiao Tong University, Dongchuan Road, Shanghai 200240, China

<sup>\*</sup> Corresponding author.

E-mail address: Cheng, H. (huanyu.cheng@psu.edu)

<sup>&</sup>lt;sup>†</sup> These authors contribute equally to this work.

tions and the exploration of bending nozzles with specific angles are also needed to ensure successful dispensing of the ink onto the surface. Unlike other direct-write printing processes, aerosol jet printing is a non-contact process where the ink droplets are jet onto the target substrate through an aerodynamic process. Although aerosol jet printing has a larger tolerance for the working distance (i.e., the gap between the printing head and target substrate), the working distance variation can also exert influence on the uniformity of the printed features [8], causing poorly defined edges and overspray [9]. Because it is an aerodynamic process, aerosol jet printing also suffers from the splash of sprinkles, which causes a fuzzy edge along the printed line. As a method to address the geometry variation in the target surface, an adaptive 3D printing method explores a closed-loop feedback system to automatically adjust the printing head position, which also allows the 3D printer to print conductive silver ink onto moving freeform surfaces [7]. However, the patterning accuracy and feature size are limited partially due to the requirement for the real-time high-accuracy scanning device. Furthermore, sintering of nanomaterials in the ink from these printing techniques often requires a high temperature. This is not compatible with the soft elastomeric substrates commonly used in stretchable/wearable electronics.

More importantly, most of these printing techniques have been explored for noble metal nanomaterials such as silver [8,10], copper [11], and carbon-based inks such as graphene [12]. The electronic waste generated as a direct result of these techniques has been increasing at an accelerated rate every year. This is causing environmental concerns and health issues as they penetrate into our ecosystem [13]. As a potential solution to mitigate or eliminate electronic wastes, transient or degradable electronics can safely dissolve in water or biofluids with environmentally friendly and biologically safe end products after their function. The demonstrated fully degradable electronics include antennas [14], printed circuit boards (PCBs) [15], epidermal sensors [16], implantable sensors [17], supercapacitors [18], and therapeutic devices [19]. This class of emerging electronics relies on a set of degradable functional materials, including conducting materials, semiconducting materials, insulating and dielectric materials. Transient metals (e.g., Zn, Mg, Mo, and W) are among the most popular composition for conductors due to their good electrical conductivities and fast water dissolution rates [20]. Zn is an important trace metal accounting for various biological functions in the human body, it has been reported to serve as the conductive material for constructing transient electronics [16]. While fabrication of transient electronics has been attempted on flat substrates either with lithographic processes or printing approaches [2,21], direct writing of transient electronics on the arbitrary freeform surface has never been achieved to the best of our knowledge.

Here we present a novel approach to directly fabricate electronics on freeform surfaces through the use of intense pulsed light-induced mass transfer (IPLMT), leveraging the evaporation–condensation effect of Zn nanoparticles [22] and intense pulsed light sintering [23]. The fabricated conductive Zn pattern can be used as conductive traces, interdigitated electrodes, sensing components, or antennas as building blocks for transient electronics on 3D freeform surfaces. Applying an

encapsulation layer on top of the transient circuits can help program the operation timeframe before their functional degradation. Traditionally, Zn-based transient electronics often require the use of vacuum-based deposition tools (e.g., E-beam evaporation or magnetron sputtering), which is time-consuming because of the associated long pumping time to achieve a high vacuum level. Due to the relatively high vapor pressure of Zn at the low-temperature range, the use of Zn in those tools may also cause contamination to subsequent samples, resulting in limited use of Zn in the tools. As an alternative, direct printing and sintering of Zn nanoparticles (Zn NPs) has been used to fabricate Znbased sensors. However, the native oxide layer on Zn NPs yields compromised conductivity [22]. Additionally, all of the existing efforts are limited to the fabrication of sensors on planar 2D surfaces. In contrast, our IPLMT method can directly and rapidly deposit Zn from the Zn NPs onto target 3D freeform surfaces in the ambient environment without a need for vacuum. The mass transfer of Zn leaves the native oxide layer behind in the Zn NPs, which leads to a significantly enhanced conductivity in the resulting Zn layers/patterns for circuit connections and sensors applications, as well as high-efficiency microwave devices. Without a need for the high-resolution scanner and motion control system (as needed in the direct 3D printing methods), the transient sensors and circuits directly printed on a 3D complicated surface via IPLMT can be achieved in a rapid and low-cost manner. The 3D devices may include electrically small antennas or be applied for smart internet-of-things. The transient circuits can also be conveniently converted into long-lasting circuits with noble metals such as Ag or Cu through a single replacement reaction by immersing the circuits into copper sulfate or silver nitrate solution followed by photonic sintering. The simple replacement process can also result in a higher conductivity in the longlasting circuits compared to that of the transient ones. The IPLMT with high-fidelity and versatility has been demonstrated by constructing various types of sensors onto freeform surfaces. Examples include glass beakers for smart Internet-of-Things (IoTs) and seashells for integration on complex biological surfaces. Because of the large-scale roll-to-roll manufacturing of printed circuits through screen printing and photonic sintering [23,24], our IPLMT method with the same setup as photonic sintering also has the potential for large-scale fabrication of printed circuits. With a pulse of 7 ms for the mass transfer process, our IPLMT method can be more competitive compared to other printing methods.

# Results and discussion

Design and investigation of process parameters in IPLMT

As shown in Fig. 1, exposure of the Zn nanoparticles (Zn NPs) to the intense pulsed xenon light (IPL) can cause light-induced heating and increase their temperature to result in mass transfer and deposition of the Zn layer on the target surfaces (Fig. 1a). Immersing the Zn patterns into a copper sulfate (CuSO<sub>4</sub>) or silver nitrate (AgNO<sub>3</sub>) solution can further convert the zinc layer into a long-lasting copper or silver layer with good conductivity after an additional photonic sintering process (Fig. 1b). Such a deposition method can be used to prepare functional circuits not only on planar surfaces but also on 3D freeform surfaces such as sea-

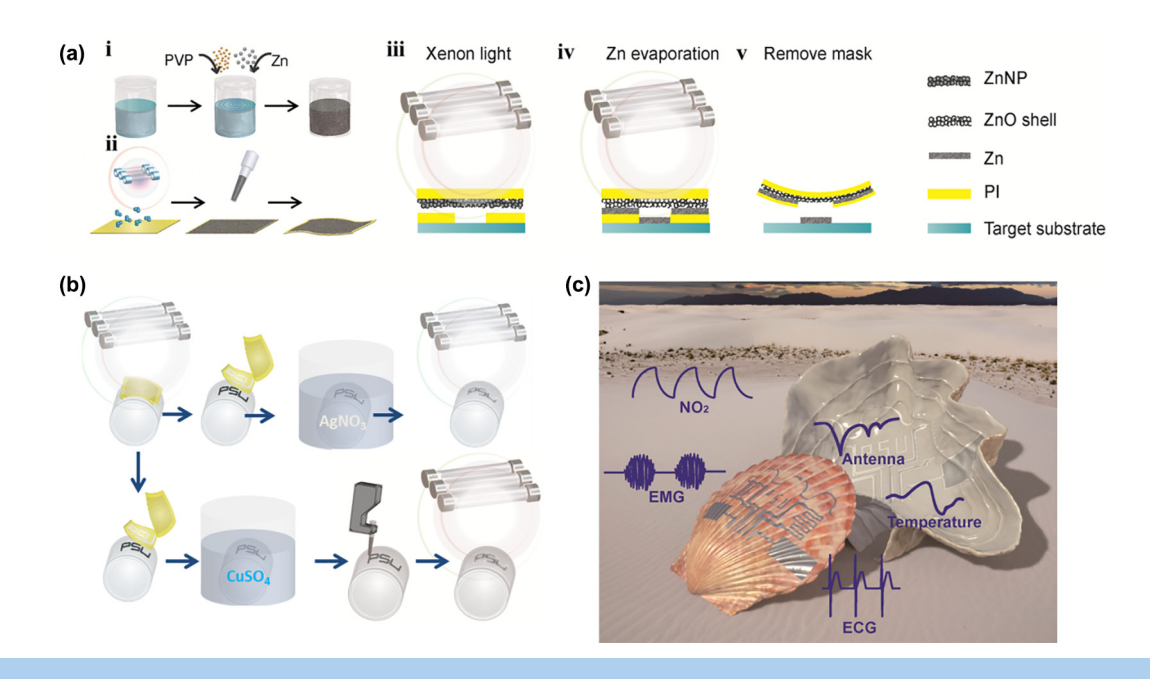


#### FIGURE 1

Schematic and demonstration of directly fabricating transient and long-lasting devices on planar and freeform substrates. (a) Schematic illustration of the fabrication process to deposit the transient Zn layer through the intense pulsed light-induced mass transfer (IPLMT) process. (i) After adding the zinc nanoparticles (Zn NPs) to ethanol with polyvinylpyrrolidone (PVP) surfactant to prepare the Zn NPs ink, (ii) dispensing the Zn NPs ink onto UV-ozone treated polyimide (PI) thin film yields a uniform coated temporary carrier layer. (iii) After applying the temporary carrier layer onto the target surface with the Zn NPs layer facing the target substrate with a sandwiched shadow mask, (iv) the intense pulsed light induces the mass transfer of Zn from the temporary carrier layer to the target substrate. (v) Removal of the shadow mask and temporary carrier layer finishes the fabrication process. (b) The transient Zn-based sensing device can be converted into a long-lasting device through a single replacement reaction of Zn with Ag or Cu formed on the 3D freeform surface such as a glass vial, by immersing the transient Zn-based device in a saturated AgNO<sub>3</sub> or CuSO<sub>4</sub> solutions. The Cu layer can also be selectively coated with another Ag NPs ink layer, followed by photonic sintering with the same intense pulsed light. (c) Multifunctional sensing circuits can be directly fabricated on a complicated 3D freeform surface such as a seashell.

shells (Fig. 1c). In brief, after applying the temporary carrier layer with the Zn NPs ink over a shadow mask pliably laminated on a freeform surface (e.g., 3D objects or complex biological surfaces), various types of sensing circuits (either transient or long-lasting) can be directly fabricated in a fast and convenient way. Smart IoTs, a network of physical objects with embedded electronics, sensors, or software that can communicate with each other, are becoming more popular as the IT revolution continues to shape the world [25]. Smart IoTs with the ability to sense, actuate, control, and respond can find wide applications in transport, healthcare, and energy [26-28]. The proposed fabrication technique is well suited to prepare sensing, communicating and even energy harvesting units on various kinds of objects with complicated shapes. The influence of various process parameters during the IPLMT of Zn was first investigated through the fabrication of Zn patterns onto a flat target surface. The fabrication of conductive Zn patterns starts with the preparation of Zn NPs ink by dispersing Zn NPs in ethanol with the help of polyvinylpyrrolidone (PVP) surfactant. As a widely used surfactant for metal nanoparticles, PVP can stabilize nanoparticles in the solvent to prevent aggregation [29]. Without the addition of PVP, the sedimentation of Zn NPs occurs in ethanol (Fig. S1). Before depositing the Zn NPs ink on the temporary carrier layer, the surface of the temporary carrier layer needs to be exposed to the UVozone treatment for enhanced wettability. Without the UVozone treatment, the Zn NPs ink deposited on the PI film exhibits significant non-uniform distribution due to the coffee ring effect (Fig. S2a). In contrast, UV-ozone treatment of the PI thin film substrate for 5 min can modify the surface wettability to facilitate a relatively uniform distribution of Zn NPs ink on the PI thin film with a thickness of 8 μm (Fig. S2b). The area or dimension of the Zn layer is currently limited by the area that the intense pulsed light (xenon) lamp is uniformly projected, which is  $15 \times 15$  cm for the lamp housing with a spiral lamp in the setup of this study. However, a larger area can be achieved with a motorized stage in a roll-to-roll configuration [30,31]. After ethanol fully evaporates, a thin layer of Zn NPs forms on the PI film (Fig. 1a-ii). To generate a specific pattern on the target substrate (e.g., glass slides), a thin-film shadow mask (e.g., dumbbell shape) prepared by laser cutting of Kapton tape is sandwiched between the glass slide and the PI temporary carrier layer with the Zn NPs ink facing inward (Fig. 1a-iii). Next, turning on an intense pulsed light instrument (Xenon light X-1100, Xenon Corp Inc) generates a strong light exposure to the Zn NPs through the temporary carrier layer within milliseconds for a total on-time of 7 ms. As shown in the output power vs time curve for the IPL equipment, the power of the IPL rapidly increases to the highest level within 1 ms followed by a sharp decrease over time (Fig. S3). The short period of exposure of the Zn NPs to the high-intensity light transiently raises their local temperature to be above their melting point, causing the evaporation of Zn beneath its surface oxide (i.e., ZnO shell) possibly through the cracks on the ZnO shell. [22] The evaporated Zn atoms then transport through the opening in the patterned

shadow mask and condense at the surface of the glass slide (Fig. 1-a-iv). Removing the Kapton shadow mask and the temporary carrier layer completes the fabrication of the conductive Zn pattern on the surface of the target substrate. Although the direct IPLMT of Ag and Cu has also been attempted by replacing Zn NPs with Ag NPs and Cu NPs, transfer of Ag or Cu is not observed, possibly due to their significantly higher melting point (961 °C for Ag and 1084 °C for Cu) compared to that of Zn (419 °C).

Such a simple yet versatile method can conveniently and quickly evaporate conductive Zn patterns onto various types of substrate surfaces, including glass slides, polystyrene (PS) Petri dishes, polyethylene terephthalate (PET) thin films, and PI thin films (Fig. 2a). The temporary carrier layer is critical because its transparency and thermal properties will affect the actual photonic energy absorbed by Zn NPs and the local temperature of Zn NPs, respectively. Since the local heating of the Zn NPs is strongly associated with the photonic energy absorbed by the Zn NPs, the energy of the IPL is also a key parameter in the process. Because of its effects on the absorbed photonic energy and heat conduction, the concentration of Zn NPs in the Zn NPs ink may also play an important role through its influence on the layer thickness of Zn NPs on the temporary carrier layer. As the

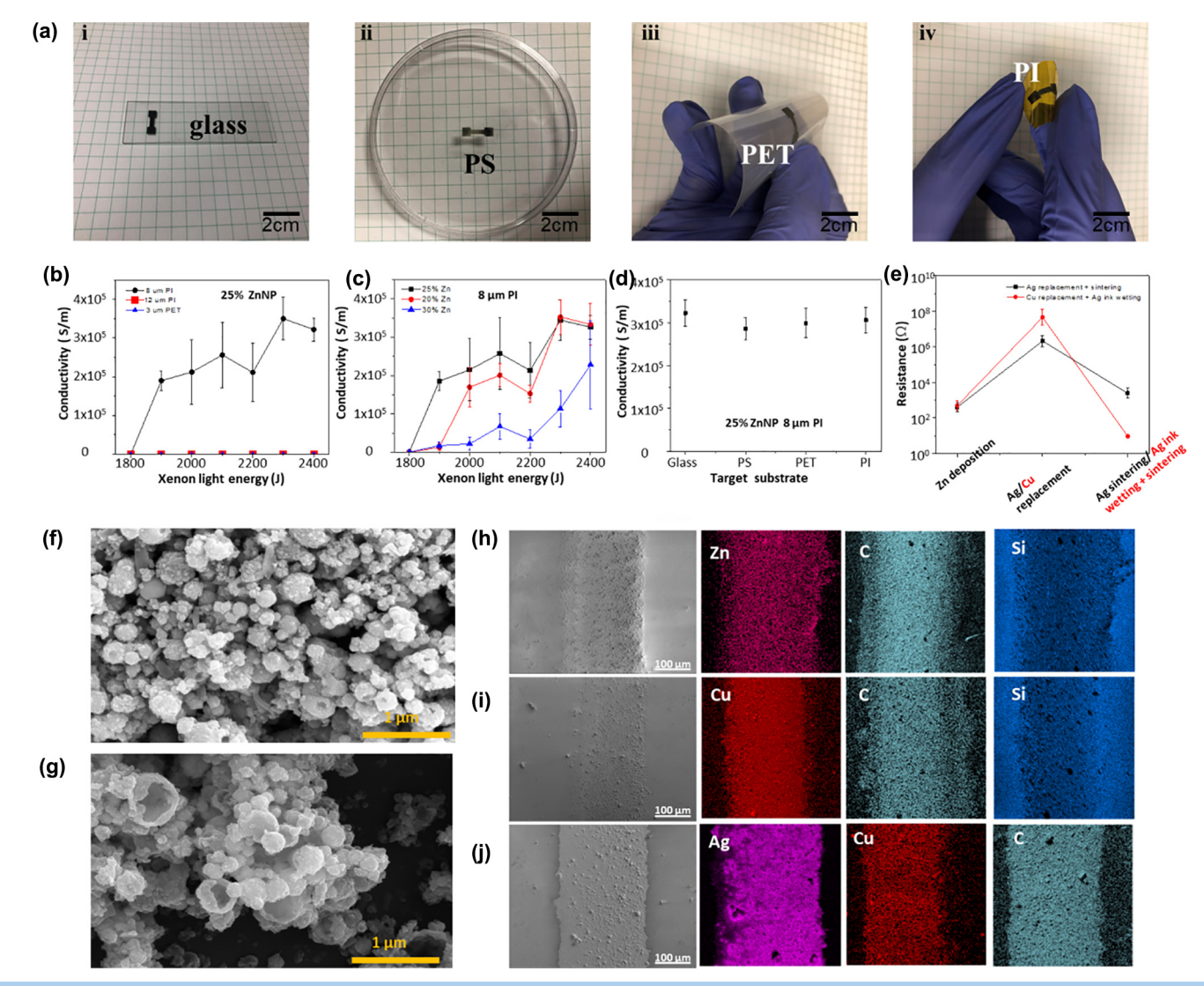


## FIGURE 2

Dependence of the electrical properties of conductive transient and long-lasting metal layers on the fabrication processing parameters. (a) Zn thin layers with dumbbell shapes are successfully evaporated onto different types of substrates, including (i) glass slides, (ii) polystyrene (PS) Petri dish, (iii) polyethylene terephthalate (PET) thin film, and (iv) PI thin film. (b) Calculated conductivity of the thin Zn layer evaporated onto glass slides from different types of temporary carrier layers, where only the thin PI temporary carrier layer with a thickness of 8  $\mu$ m yields successful Zn evaporation with a gradually increased conductivity as the exposure energy from xenon light increases. (c) Calculated conductivity of the thin Zn layer evaporated onto glass slides from the Zn NPs inks with different concentrations of Zn NPs. (d) The conductivity of the Zn layer evaporated to different types of target substrates is ca.  $3 \times 10^5$  S/m, showing negligibly small differences among target substrates. (e) Resistance evolution of the conductive lines from the Zn layer to intermediate substituted Ag or Cu layer and finally to the sintered Ag layer. Scanning electron microscopy (SEM) images of the PI temporary carrier layer (f) before and after (g) IPLMT of Zn, which highlights hollow spheres of Zn NPs on the PI temporary carrier layer post-exposure to intense pulsed light. SEM and energy-dispersive X-ray spectroscopy (EDX) images of (h) the Zn layer evaporated on glass vial, (i) the Cu layer formed by a single replacement reaction in the evaporated Zn layer in the CuSO<sub>4</sub> solution, and (j) the Ag layer further formed by coating Ag NPs ink on the Cu layer followed by photonic sintering.

electrical conductivity is key to the conductive circuits and resistance-based sensors, we first investigate the effect of these three parameters on the electrical conductivity separately in the experiment. The calculation of the electrical conductivity of the IPLMT-evaporated Zn layer is based on its electrical resistance value and dimensional parameters. After evaporating the Zn pattern in a dumbbell shape with a neck width of 4 mm and a neck length of 10 mm on the target substrate by the IPLMT method, its resistance is measured by a digital multimeter. An optical profilometer (Zygo) scans the thickness and confirms the width of the Zn pattern (Fig. S4). The effect of the temporary carrier layer on the electrical conductivity of Zn pattern is demonstrated through the use of three different temporary carrier layers, namely PI films of 8  $\mu$ m, PI films of 12  $\mu$ m, and PET films of 3 µm (Fig. 2b, 10 samples in each group). As the xenon light energy gradually increases from 1800 J to 2400 J, the electrical conductivity of the evaporated Zn layer on the PI thin films of 8  $\mu m$  increases from 0 S/m to 3.2  $\times$  10<sup>5</sup> S/m. Because of the significantly high local temperature even just at the Zn/PI interface, the PI thin film of 8 µm slightly crumples from an initially flat shape after the xenon light exposure (Fig. S5a). In contrast, the PI films of 12 μm are unable to generate the conductive Zn pattern at all levels of xenon light energy, due to the significantly attenuated photonic energy from their larger thicknesses and increased opacity (Fig. S6) and larger heat capacity compared to PI films of 8  $\mu$ m. The previous literature report [32] indicates that the ZnO NPs with a diameter of 40 nm have a light absorption peak at 361 nm and the light absorption gradually decreases as the wavelength increases. Due to the existence of the native oxide on the surface of Zn NPs, it is reasonable to conclude that the transmittance difference in the PI films with different thicknesses can affect the total energy absorbed by the Zn NPs. This observation also helps explain the failure of the IPLMT process using the 12  $\mu m\text{-thick}$  PI carrier layer. This postulation is further confirmed by the observation that the Zn NPs layer on the PI films of 12 µm remains unchanged after the IPL exposure (Fig. S5b). The significantly attenuated photonic energy from the temporary carrier layer can result in a lower local temperature of the Zn NPs such that the evaporation of Zn atoms is not favorable. While the clear PET films of 3  $\mu m$  are associated with increased light transmittance and decreased heat capacity, no successful Zn evaporation appears over the wide range of xenon light energy, and the PET thin film is burned into ashes when the xenon light energy level is above 2200 J (Fig. S5c). Such unsuccessful results may be ascribed to the significantly low glass transition temperature of the PET compared to that of the PI [33]. The wavelength spectrum of the xenon lamp in X-1100 confirms the presence of deep UV at around 200 nm wavelength with high intensity (Fig. S7). In addition to ZnO that can absorb most energy of the UV from 200 to 400 nm [34,35], Zn interstitial rich honeycomb nanostructures of ZnO show improved absorption in deep UV [36]. Due to the ultraviolet-photoelectric effect [37], deep UV could generate Zn ions for increased absorption of deep UV [36]. Because deep UV radiation can reduce the electron transfer resistance in a ZnO nanosheet from photonic sintering [38], its effect on the material transfer process is further investigated by using a transparent UV filter sheet (Edmund Optics). After applying the UV filter to block the UV light exposure, the Zn NPs are not uniformly transferred and the mass transfer is not successful in  $\sim$ 50% of the target area (Fig. S8).

The investigation of the effect of Zn NPs concentration involves the use of the Zn NPs ink with three different Zn NPs concentrations (i.e., 20%, 25%, and 30%) prepared and dispensed on the PI film of 8 µm. Gradually increasing the power of the xenon light results in increased conductivity of the deposited Zn layer for all three types of Zn NPs ink. The Zn NPs ink with a concentration of 25% or 20% exhibits a significantly higher conductivity than that of 30% (Fig. 2c). Such a phenomenon may result from the difference in the Zn NPs layer thickness. As measured by the optical profilometer, the thickness of the Zn NPs layer on the PI thin film increases from 3 µm to 7 µm as the concentration of the Zn NPs ink increases from 20% to 30% (Fig. S9). Because the photonic energy is mainly absorbed by the Zn NPs close to the Zn/PI interface, a thicker Zn NPs layer impedes the escape of Zn atoms from inside to the top surface. To further verify this hypothesis, Zn NPs layers with different thicknesses are used for the IPLMT process by applying different numbers of drops (1, 2, and 3, with a volume of 5 µL in each drop) of the Zn NPs ink with a concentration of 25% on the temporary PI carrier layer. The Zn NPs layers formed by two or three drops of the ink are not able to generate a conductive Zn pattern even when the xenon light energy is increased to the maximum (Fig. S10a). This observation is likely due to the reduced optical absorption in the thicker Zn NPs layer [39], because the thickness of the Zn NPs layer measured by the optical profilometer significantly increases from 4 µm to 50 µm as the Zn NPs ink droplet increases from 1 to 3 (Fig. S11). The thickness of the transferred Zn layer is determined through an optical profilometer and it depends on both the number of cycles in the Zn mass transfer process and the thickness of the Zn NPs layer. The transferred Zn layer thickness firstly achieves a peak around 300 nm when the thickness of the Zn NPs layer on the carrier PI substrate is ~4 μm (Fig. S12). The results indicate that under the same condition of IPL and the carrier substrate, increasing the amount of Zn NPs doesn't necessarily increase the thickness of transferred Zn. On the other hand, as the thickness of the Zn NP layer continue to increase to ~50 µm, the thickness of the transferred Zn layer increases to another peak value of ~500 nm, possibly due to the excessive amount of Zn source. Increased Zn layer thickness is also observed when multiple Zn transfer cycles are performed (Fig. S13). It should be noted that no improved conductivity is observed for either the Zn layer transferred from the ~50 μm thick Zn NPs layer or multiple exposure cycles, which may be related to the impurities caused by the thermal decomposition of PVP and PI. Further investigation is needed to fabricate a thicker Zn layer and promote its electric conductivity through IPLMT. While the highest conductivity of the Zn layer from the IPLMT process (i.e.,  $3.5 \times 10^5$  S/m) is about 2% of its bulk counterpart (i.e.,  $1.81 \times 10^7$  S/m), it is already 15% of sputtered Zn ( $2.3 \times 10^6$ ) and 35% of E-beam evaporated Zn  $(1 \times 10^6)$  (Fig. S10b). Such a conductivity of the Zn layer from the IPLMT process ranks top among other fabrication processes for Zn-based transient electronics (Table S1). Nevertheless, no significant difference of conductivity is observed for the Zn layers deposited onto a variety of different target substrates, including glass, PS, PET, and PI, indicating the versatility of the

IPLMT process (Fig. 2d). The adhesion of the IPLMT transferred Zn layer on the glass slide is investigated by applying a commercial 3 M scotch tape on the Zn layer in the peeling test (Fig. S14). The transferred Zn pattern remains intact after multiple cycles of the peeling and its resistance only increases by 0.34% after 20 consecutive peeling cycles. Additionally, the sharp increases in the resistance of the transferred Zn layer are associated with the incidences when the pressure is applied onto the 3 M tape. While the adhesion of the transferred Zn layer on the target surface is robust as indicated by the negligibly small resistance change, it is interesting to note the pressure-sensitive properties of the transferred Zn layer, possibly due to pressure-induced morphology change. The hardness of the transferred Zn layer is not evaluated due to its ultrathin thickness, uneven surface morphology, and the limitation of the currently available nanoindentation tool, but it will be investigated in future studies. In summary, the above results indicate that the IPLMT of Zn is a fast and simple method for fabricating Zn-based transient electronics, which addresses the challenges of lithographic processes and printing approaches. In the following discussion, the Zn NPs ink with a concentration of 25 wt% on the temporary PI carrier layer of 8 µm exposed to a xenon light energy of 2400 J is used in the IPLMT of Zn for device fabrication unless otherwise specified.

The dissolution of the Zn from the IPLMT process is first investigated to reveal its functional degradation. The demonstration involves the use of a glass vial as the target surface. Because the dissolution rate of Zn is relatively fast, the Zn-based electronics can only operate for less than hours before breakdown after their immersion in water. Though such a quick dissolution process makes Zn an ideal material candidate for devices with temporary use purposes, the oxidation of Zn happens quickly in the ambient environment. The long-lasting Ag electrodes exhibit a much smaller variation in the resistance than that of the transient Zn electrodes (Fig. S15), indicating the need for an encapsulation layer as in the previous study [40]. As a demonstration, Znbased resistors are fabricated with the IPLMT on the outer surface of a glass vial, with one encapsulated by a water barrier layer (PDMS) and the other without. The encapsulation layer can also exploit degradable polymers, including poly(lactic-co-glycolic acid) (PLGA) [41], poly(alkyl cyanoacrylate) (PACA) [42], poly (ε-caprolactone) (PCL) [43], and galactomannan [16]. After the resistors are immersed in water at room temperature, their resistances are constantly monitored by a digital multimeter to inform the degradation process (Fig. S16a). While the Zn-based resistor without encapsulation can only function for ca. 40 min after immersion in water (followed by a gradual increase in the resistance to indicate its breakdown), the resistor with encapsulation shows negligible resistance change during the test (Fig. S16b). Easy removal of the Zn-based sensors (without encapsulation) is also demonstrated by wiping off the sensor with gloves after taking it out from the water (Fig. S16c-d). While the PDMS layer is used as an encapsulation layer in this demonstration, it can be easily replaced with other transient or biodegradable thin films, whose thickness or choice can help program the operation time of Zn-based transient electronics [44]. The transient sensors based on the Zn from the IPLMT process exhibit high-fidelity performance, comparable with their

commercial counterparts. The demonstrated examples include sensors and electrodes to monitor electrophysiological signals such as the electrocardiogram (ECG) and electromyogram (EMG). After depositing the Zn pattern from the IPLMT process on polyvinyl alcohol (PVA) thin films, the sensors can be pliably attached to the skin surface. The pliable attachment with a strong adhesion is achieved through a partial dissolution and softening of the PVA thin film to conformally adhere to the textured skin surface. The successful deposition of the Zn on the PVA thin film changes its surface roughness, as shown by SEM images before and after the deposition (Fig. S17ab). The partial dissolution of the PVA beneath the transient electrodes indeed replicates the microstructures of the skin surface (Fig. S17c), further confirming the conformal contact between the electrode and skin. The ECG and EMG signals are collected in the ambient environment with the healthy human subject sitting on a chair. A commercial biopotential data acquisition system (Powerlab, ADInstruments) is used with recommended settings (0.5-100 Hz bandpass filter for ECG and 20-500 Hz bandpass filter for EMG) at a sampling rate of 1 kHz. The improved contact quality at the electrode/skin interface ensures a good signal-to-noise ratio (SNR) for both ECG and EMG signals (19.74 and 8.52, respectively) (Fig. S18). The SNR is calculated following the definition:  $SNR = 20\log(V_s/V_n)$ , where  $V_s$  is the peak-to-peak value (between the R peak and S peak of the PQRST wave in the ECG signal) and  $V_n$  is the peak-to-peak value of the noise [16]. After use, the transient sensor easily detached from the skin surface slowly dissolves in water and completely disintegrates after 24 h of soaking at the room temperature (Fig. S19).

Fabrication of electronics on a smooth surface for smart IoTs Though the thickness and choice of the encapsulation layer can program the operation time for Zn-based transient electronics, demand still exists for long-lasting electronics on a 3D freeform surface for smart contact lens, smart IoTs, and non-planar devices [4]. As a step toward such a need, we then demonstrate the viability of the IPLMT process to pattern noble metals such as copper (Cu) and silver (Ag) on a 3D freeform surface. However, this seems challenging because the IPLMT of Cu or Ag is not successful when Zn NPs inks are switched to Cu NPs or Ag NPs. The unsuccessful evaporation of the Ag and Cu NPs by the IPLMT may likely result from the elevated melting temperatures of Ag of >1200 K [45] and Cu of >825 K [46] compared to that of Zn of >700 K when their sizes are similar (~70 nm). In order to address this seemly challenging task, the single-replacement reaction has been explored to replace the evaporated Zn layer with Ag or Cu. As a demonstration, the patterned Zn layer is first prepared onto a glass beaker by the IPLMT method. The substitution of Zn with Ag or Cu has then been achieved by immersing the target substrate with Zn patterns in the saturated silver nitrate (AgNO<sub>3</sub>) and copper sulfate (CuSO<sub>4</sub>) solution for 1 min. While the Zn pattern can be successfully replaced by Ag or Cu, a significant resistance increase is observed, possibly due to the loose interconnection between the Ag or Cu dendrite formed during the single replacement reaction (Fig. 2). Such a compromised conductivity is not favorable in constructing conductive traces for long-lasting electronics. Because photonic sintering with intense pulsed light has been widely used to induce rapid heating of metal NPs and nanowires [47,48] for sintering, the same setup used for the IPLMT process can be used for photonic sintering of the formed Ag or Cu dendrite [49]. In fact, photonic sintering of the replaced Ag layer by a xenon light energy of 900 J has successfully decreased the resistance by three orders of magnitude (from  $\sim 2.0 \text{ M}\Omega$  to  $\sim 2.5 \text{ k}\Omega$ ) (Fig. 2e). Other than direct sintering of the noble metal dendrite, coating of the Ag NPs ink (JS-A191, Novacentrix) on the replaced Cu layer can also be achieved through a picoliter dispenser (Microplotter, Sonoplot) due to the increased wettability (Fig. S20) of the Cu dendrite layer. Sintering of the coated Ag NPs ink on top of Cu results in resistance of less than  $10 \Omega$  that is much lower than the original Zn layer and the replaced Ag layer. To help reveal the underlying mechanism behind the IPLMT process and the subsequent replacement reaction, scanning electron microscope (SEM) images have been taken for both the temporary PI carrier layer and the target surface. Compared to the solid Zn NPs before their exposure to intense pulsed light (Fig. 2f), hollow spheres of the NPs observed (Fig. 2g) on the temporary PI carrier layer after the IPLMT process imply the evaporation of the Zn in the core of the NPs beneath their native oxide shells. In addition to Zn on the glass (i.e., Zn and Si signals), carbon (C) is also observed on the target glass substrate as shown in the energy-dispersive X-ray spectroscopy (EDX) mapping (Fig. 2h), possibly due to the decomposition of the PVP and PI. The decomposition of the PVP and PI starts to occur at a temperature of 250 and 500 °C, respectively. The decomposition of PVP under the irradiation of IPL has been previously reported, [50] whereas the decomposition of PI needs further investigation. To confirm the source of the C residue on the glass surface also comes from the PI, Zn NPs ink without the PVP additives is also used for the IPLMT. XPS analysis reveals the chemicals transferred to the target substrate from two types of Zn NPs inks: one with and the other without PVP additives (Fig. S21). The nearly identical spectra of the two samples both show the existence of carbon residues, indicating the decomposition of the PI. It should also be pointed out that the amount of PVP added to the Zn NPs ink is only 0.1 wt% to provide a limited amount of C source. SEM of the PI film after IPL exposure was also carried out (Fig. S22). Holes on the PI film after the IPLMT process suggests the melting of the PI film. Hollow spheres are also observed for the Zn NPs without the addition of PVP, indicating that the existence of hollow spheres is not caused by the PVP decomposition (Fig. S23). A similar hollow structure has been previously reported after heating of Zn NPs in the TEM chamber [42] or the laser scanning of Zn NPs [22]. The formation of the hollow spherical structure is also associated with the drop in the ratio of Zn to O from 2.56 to 1.38, as characterized by the EDX mapping. These observations indicate the escape of Zn atoms in the core of Zn NPs through the preexisting cracks of the ZnO shell, which results from the mismatch in the coefficients of thermal expansion between Zn and ZnO during the heating process. The Zn evaporation and PI decomposition also partially support the existence of transient high temperature at the Zn/PI interface. After immersion of the Zn layer in the CuSO<sub>4</sub> solution, the Cu layer is then confirmed by the EDX with the C layer remaining on the glass (Fig. 2i). The Zn is not fully replaced by Cu, as the element of Zn residues is still observed after the replacement reaction in the EDX mapping (Fig. S24). Following the coating and photonic sintering of the Ag NPs ink, a conductive single line a width of 200  $\mu$ m exhibits well-defined edges for the composition of C, Cu, and Ag. The well-defined feature at the edge comes from the significant difference in surface wettability between the replaced Cu layer and its surrounding area of glass for spontaneous wicking of the Ag NPs ink (Fig. 2j).

A system-level demonstration of the multifunctional electric

circuit on a 3D glass beaker consists of a dipole antenna, electrodes for ECG measurements, humidity sensor, temperature sensor, and their corresponding pads for connection. After laminating the kirigami-patterned soft semi-transparent PI film with Zn NPs on both the bottom and side surfaces of the glass beaker, carrying out multiple exposures through the IPLMT of Zn deposits Zn onto both the bottom (Fig. 3a) and sidewall (Fig. 3b) of a glass beaker. The follow-up Ag NPs replacement and photonic sintering processes further convert the transient Zn device into the long-lasting Ag device, resulting in a smart beaker. The performance of each sensing element in the multifunctional circuit compares favorably against their commercial counterparts. Contact impedance between the electrodes and human skin is first analyzed by an LCR meter (Hewlett Packard 4284A) from 20 Hz to 2 MHz (Fig. 3c). When compared to the commercial gel electrodes, a higher contact impedance is observed from the electrodes, which is consistent with previous literature reports on metal-based ECG electrodes [16]. Placing two thumbs on the electrodes on the 3D glass beaker enables the real-time monitoring of the ECG signal from the human subject through a data acquisition system (ADInstruments). A comparison of the ECG signals collected from the smart beaker and commercial gel electrodes attached to the wrist of the human subject indicates a slight baseline shift from the former, likely ascribed to the changing contact impedance at the electrodes/thumbs interface (Fig. 3d). Though the ECG signal from the smart beaker exhibits a slightly smaller signal-to-noise ratio (SNR) compared to that of the commercial gels, the PQRST wave is still evident and sufficient for clinical diagnostics. The humidity sensor on the smart beaker involves the use of ZnO NPs drop-cast on an interdigitated electrode (IDE). Calibration and testing of the humidity sensor have been accomplished by placing the smart beaker inside a controlled chamber with a given relative humidity (RH) level (i.e., 49% RH, 55% RH, 59% RH, 66% RH, or 72% RH) for 2 min. The humidity sensor on the smart beaker linearly increases with the increasing RH level with a sensitivity of 0.51%/RH% (Fig. 3e). The humidity sensor also exhibits a good response (~2 min) and fast recovery rate (<20 s) at room temperature (Fig. 3f). With either conductive Zn or Ag lines, the ZnObased humidity sensor fabricated with the IPLMT method is exposed in a humid environment (75% RH at room temperature) over five days to demonstrate the stability of the humidity sensor (Fig. S25). The one with conductive Ag lines shows a smaller variation in the relative resistance than that with conductive Zn lines, indicating the rate of oxidation in the conductive Zn lines and also the need for an encapsulation layer as in the previous study [40]. In the perturbation test, opening the lid of the chamber to the open air for different durations reduces the humidity in the chamber and resistance of the sensor, followed by a recovery after closing the lid (Fig. S26). The time interval of 3 h

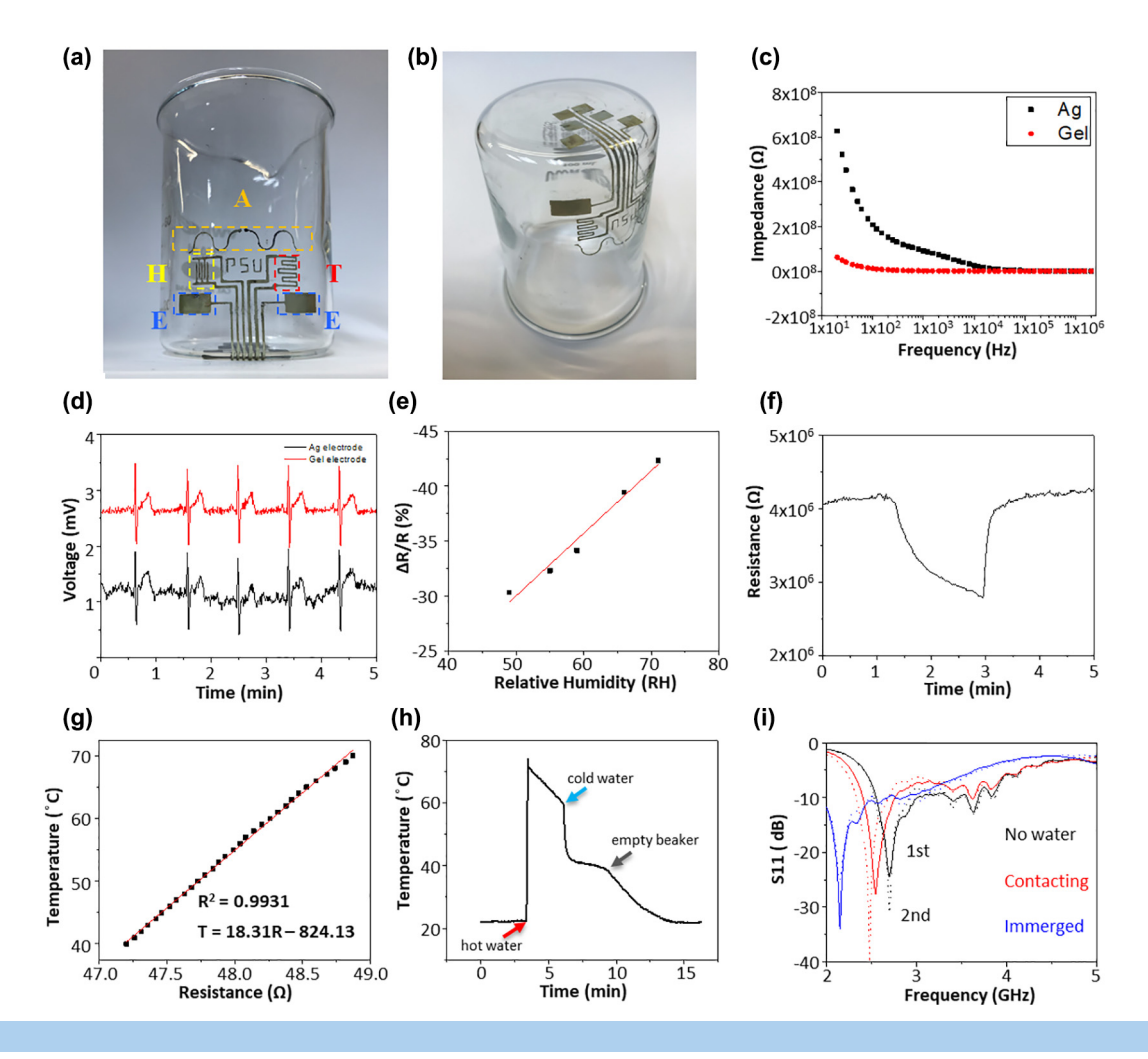


# FIGURE 3

Multifunctional sensing circuits fabricated on the sidewall and bottom surfaces of a glass beaker toward smart Internet-of-Things (IoTs). Photographs of (a) multifunctional Ag-based sensing circuits on the sidewall and (b) their contact pads (for external connections) patterned on the bottom surface of the glass beaker. A: antenna; H: humidity sensor; T: temperature sensor; E: electrode to measure electrophysiological signals. (c) Contact impedance measured by the Ag electrodes and gel electrodes that are in contact with two thumbs from a human subject. (d) Comparison of the electrocardiogram (ECG) signals captured by Ag electrodes on the beaker and commercial gel electrodes. (e) Sensitivity of ZnO-based humidity sensor and (f) its representative humidity sensing curve. (g) Calibration curve of the Ag-based temperature sensor and (h) its recorded temperature change of the glass beaker after the addition of hot water. (i) Shift in the resonance frequency of the dipole antenna as the water is gradually added to the beaker from empty (black) to contacting the dipole antenna (red) and then to completely immerging the dipole antenna (blue).

between cycles ensures the recovery of 75% RH in the chamber. When the Zn layer on the glass slide is repeatedly moved onto and away from the hot plate to vary the temperature between 23 and 35 °C, the resistance variation at room temperature (23 °C) is less than 4% (Fig. S27). After obtaining the linear calibration curve between the resistance and the temperature by filling the beaker with hot water (Fig. 3g), the temperature sensor can detect the temperature change as hot water is poured into the beaker and keep track of the cooling process (Fig. 3h). In addition to its future use for wireless communication and RF energy harvesting, the antenna located at the middle of the sidewall on the smart beaker is also able to detect the level of water in the beaker. The resonance frequency of the dipole antenna shifts to a lower value as water is filling up the beaker (Fig. 3i) due to the change of the permittivity in the dielectric environment. Compared to the direct patterning of noble metal NPs ink on the curved surface through 3D printing, the IPLMT-based method is more rapid, low-cost, and efficient because it does

not require a high-resolution scanner and motor control system as those used in the direct printing methods. The key aspect is that the difference in surface wettability between the replaced Cu and the surrounding areas allows the Ag NP ink to directly wet and quickly spread the replaced Cu pattern with clearly defined edges due to the capillary force.

Fabrication of electronics on complicated biological structures. Though the successful fabrication of circuits on a 3D glass beaker demonstrates the potential of IPLMT for smart IoTs, the application of IPLMT on biological surfaces can still be challenging due to their complicated surface morphologies. Biological surfaces that have been explored to integrate sensing circuits include flower pedals [51], leaves [52], and wood [53]. The applications for directly fabricating circuits on these biological surfaces range from environmental monitors to devices with wireless communication modules. By using a leaf sensor, farmers would be able to track the biochemical processes of their crops in real time [52].

Many industries could also benefit from ultra-high frequency (UHF) radio frequency identification (RFID) tags fabricated on wood to allow for battery-free tracking of objects [53]. As a good candidate for biological structures, seashells are selected here to demonstrate the feasibility and performance of the IPLMT process on complicated freeform surfaces. The same set of transient Zn circuit components as above has been fabricated on the complex surface of a seashell using the IPLMT method. Due to the complicated shape of the seashell and large curvature changes, the shadow mask based on a thermal release tape double layer does not conform to the surface of the seashell due to the compromised flexibility of the thermal release tape with a large thickness. To ensure good contact between the shadow mask and seashell, the Kapton tape is retrieved from the thermal release tape to reduce the thickness before application to the surface of the seashell. Fig. 4a shows the photograph of the Zn layer deposited on the surface of a seashell. The granular morphology of the Zn deposited by the IPLMT process is similar to that of Zn from sputtering or e-beam evaporation (Fig. S28). It should also be noted that the resolution of the transferred Zn pattern is rela-

tively low mainly due to the limited resolution of the Kapton tape shadow mask fabricated by CO2 laser cutting. However, it is possible to exploit a higher-resolution laser cutting tool (e.g., UV or femtosecond laser) to prepare the shadow mask for reducing the feature size of the transferred Zn pattern. Since the seashells have numerous grooves on their surfaces (Fig. S29), selective wetting of the Ag NPs ink on the seashell surface is not successful due to the uncontrollable flow of the Ag NPs ink along the grooves. The single replacement reaction of Zn in the AgNO<sub>3</sub> solution is explored to convert the Zn pattern into Ag, followed by photonic sintering (Fig. 4b). As observed in the SEM images, densification of the sintered Ag in the formed large silver films exhibits a similar morphology as those thermally sintered [54]. To verify the functionality of the Ag-based circuit directly patterned on the seashell, the performance of a gas sensor based on an IDE and a temperature sensor has been examined. The gas-sensitive rGO/MoS2 composite nanomaterial synthesized by the solvothermal method as described previously [55] is dispensed on the IDE to construct a NO<sub>2</sub> gas sensor. The responses of the gas sensor gradually increase as the

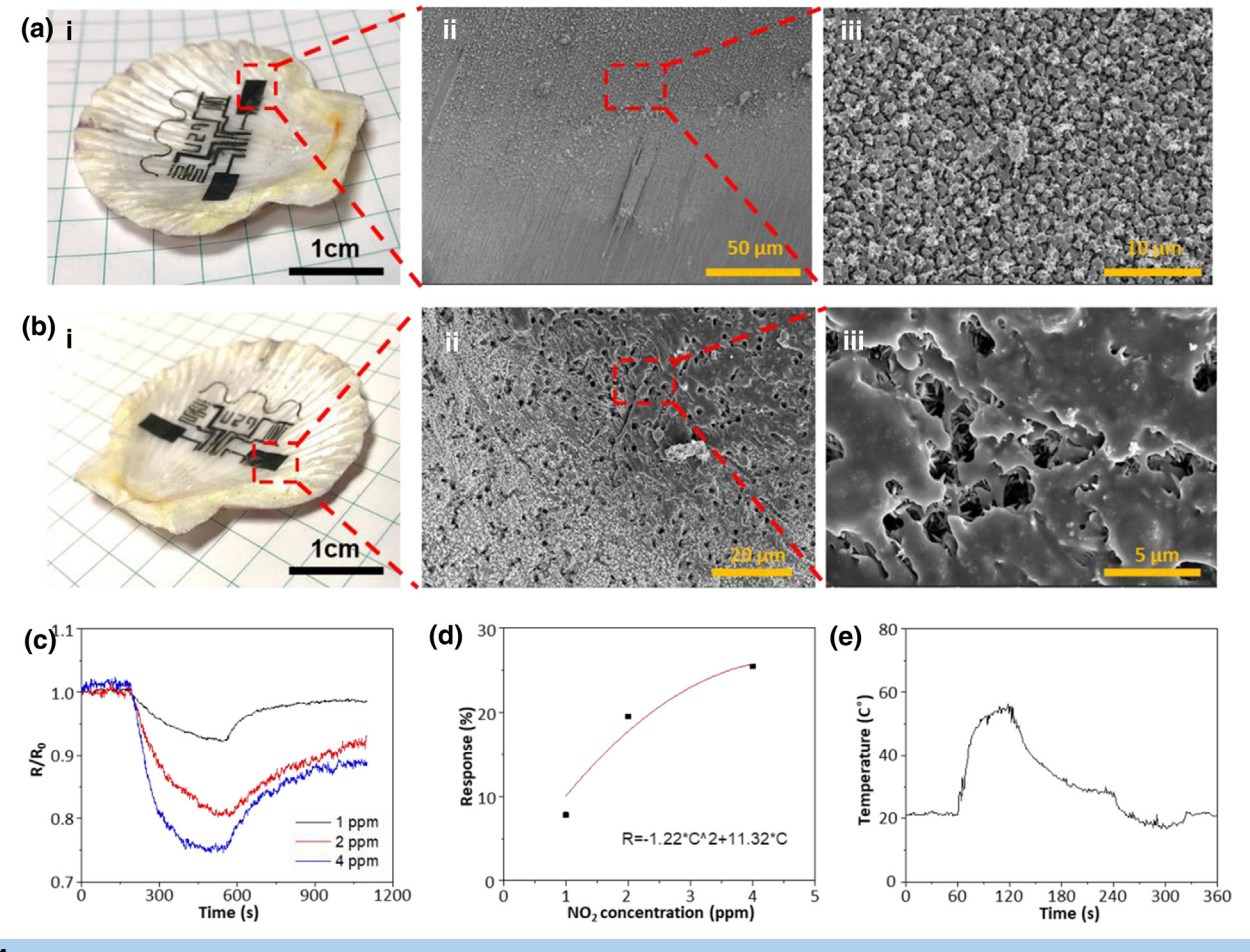


FIGURE 4

Multifunctional sensing circuits patterned on a seashell as a representative biologically complex surface. (a) (i) Optical image and (ii) SEM image of the Zn layer patterned on the seashell with (iii) the magnified SEM image showing the granular shape of the deposited Zn. (b) (i) Optical image of the Ag layer formed on the seashell by a single-replacement reaction after immersing the Zn-based device in a saturated  $AgNO_3$  solution. (ii) SEM image and (iii) its magnified view to show the morphology of the Ag layer on seashell after photonic sintering and the large Ag film formed by the densification of Ag NPs. (c) Sensing response curve of the  $Ag NO_3$ -based  $Ag NO_3$  sensor to  $Ag NO_3$  and 4 ppm at room temperature. (d) Sensitivity of the  $Ag NO_3$ -based  $Ag NO_3$  sensor follows the power law of chemiresistive gas sensors. (e) Temperature change of the seashell recorded by the temperature sensor during the heating and cooling processes of seashell induced by continuous air blowing.

concentration of NO2 increases from 1 to 4 ppm at room temperature (Fig. 4c). The slow and relatively incomplete recovery of the signal can be addressed by adding a heating element to increase the working temperature of the rGO/MoS<sub>2</sub> sensing material, as in our previous work [56]. A polynomial fitting curve with a diminishing slope toward a higher concentration of NO<sub>2</sub> agrees well with the power law of chemiresister-based gas sensors (Fig. 4d). The temperature sensor with a sensitivity of  $0.055 \,\Omega/^{\circ}C$  can track the heating and cooling of the seashell by an air blower (Fig. 4e). The seashell is first placed at room temperature for 1 min before blowing hot air. A sharp increase and a slow decline of the seashell temperature are observed during the hot air blowing of 1 min and the cooldown process of 2 min, respectively. The blowing of cool air for 1 min after the natural cooling process further decreases the temperature of the seashell. Both the gas sensor and the temperature sensor show more fuzzy signals compared to their counterparts fabricated on the glass beaker. It is highly possible that the reduced or non-uniform conductivity of the Ag conductive trace formed by the single-replacement reaction introduces a higher level of noise relative to the signal, causing degraded performance of the sensors.

# Conclusion

We have reported a novel IPLMT process to deposit Zn for constructing transient circuits onto various types of flat and nonflat 3D freeform surfaces. After elucidating the effect of various processing parameters on the performance of the IPLMT Zn, the optimal set of parameters has been identified to yield highly conductive Zn patterns for fabricating electronics on 3D complicated surfaces. The single-replacement reaction and/or selective coating of the Ag NPs ink has also been explored to convert the patterned Zn layer into long-lasting Cu or Ag. The versatility of this powerful method has been showcased through a systemlevel demonstration with electronics that include antennas, electrodes, temperature sensors, and gas sensors on 3D surfaces for smart IoTs and integration on complicated biological surfaces. This novel method can generate circuits on complicated surfaces with well-controlled yet small feature sizes, overcoming several obstacles faced by traditional lithographic processes or various advanced printing approaches. As a result, the IPLMT process possesses a huge potential to create novel transient and longlasting devices and systems for applications in a variety of fields including optoelectronics, telecommunication, and medicine.

# **Experimental section**

# Preparation of the Zn NPs inks

PVP of 0.0025 g was first added to ethanol of 2 g in a glass vial followed by a 15 min sonication to thoroughly dissolve the PVP. After the PVP was fully dissolved in ethanol, Zn NPs (35–45 nm, US Research Nanomaterials) of 0.5 g were added into the glass vial with sonication to ensure good dispersion of Zn NPs in the solvent, yielding the Zn NPs ink of 20 wt%. The Zn NPs inks with other concentrations of Zn NPs or Zn NPs without PVP were prepared using the same procedure with corresponding concentrations of Zn NPs or without the addition of PVP.

# Preparation of the PVA substrate

The PVA thin film substrate was first prepared by dissolving PVA powder of 3 g (Sigma-Aldrich) in deionized water of 27 g, followed by stirring for 2 h at 90 °C and then tape casting on glass slides. The doctor blade coating was used to control the thickness of the PVA thin film to be 40  $\mu m$ . Placing the film at room temperature for 2 h fully evaporated the water and cured the PVA thin film.

#### IPLMT of Zn thin film on flat surfaces

Target substrates (e.g., glass, PS, PET, PI, or PVA) were first cleaned with ethanol before the IPLMT process. Next, the Zn NPs ink was applied onto the temporary carrier layer (i.e., 3  $\mu$ m-thick PET, 12  $\mu$ m-thick PI, and 8  $\mu$ m-thick PI films) after the temporary carrier layer was exposed to UV-ozone (UV10 Ozone cleaner system, Novascan Technologies, Inc) for 5 min. After aligning the temporary carrier layer with the target substrate, a height-adjustable stage was used to bring the samples close (<1 cm) to the xenon light (X-1100, Xenon Corp, Inc) for IPLMT. The thickness of the ZnNP layer and the transferred Zn layer was measured by an optical profilometer (Zygo) (Figs. S30–34).

# SEM imaging

SEM images were taken by Verios XHR SEM (Thermal Fisher Scientific, Inc). The Iridium layer of 5 nm was coated on the top surface of the samples to prevent the potential charging effect.

# Fabrication of sensing circuits on glass beaker

A shadow mask was first fabricated by patterning a Kapton tape with a commercial CO<sub>2</sub> laser (Universal Laser Systems). Briefly, a Kapton tape with a thickness of 25 µm and the adhesive facing outward was carefully aligned on the thermal release tape (REVALPHA, Nitto) to avoid trapped air bubbles. The thermal release tape functioned as a temporary substrate to keep the Kapton tape flat during the laser patterning process. After generating a predefined pattern in AutoCAD, a CO<sub>2</sub> laser (power: 7%, speed: 4%) was used to pattern the Kapton tape. Peeling off the excessive region yielded the shadow mask. Next, the Kapton shadow mask was taped onto the glass beaker. Heating the thermal release tape with a hot air blower left the shadow mask onto the target substrate and completed the transfer printing process of the shadow mask. After fixing the Zn NPs ink on the PI temporary carrier layer over the Kapton shadow mask on the glass beaker with tapes, xenon light was applied to initiate the IPLMT of Zn NPs. Removal of both temporary carrier layer and shadow mask finished the IPLMT of Zn. The substitution of Zn with Ag or Cu was achieved by immersing the Zn pattern on the glass beaker into saturated AgNO<sub>3</sub> or CuSO<sub>4</sub> solution for 1 min. After converting the Zn into Cu through the single replacement reaction, a picoliter dispenser (Microplotter II, Sonoplot) was used to selectively coat the conductive pattern with AgNP ink due to its enhanced wettability. The glass tip with a diameter of 20  $\mu m$ attached to a piezoelectric motor from the Microplotter ensured both precise control of the contact location and continuous flow of AgNP ink. Photonic sintering (energy: 900 J) was then used to fully sinter the coated AgNP to yield the final functional sensing circuit on the glass beaker.

## Fabrication of circuits on a seashell

The Kapton shadow mask was first fabricated following the same procedure as previously described. A small amount of ethanol was applied to the surface of the seashell before placement of the shadow mask that was first retrieved from the thermal release tape. The surface tension between the ethanol solution and shadow mask helped bring the shadow mask to the proximity of the seashell surface after the ethanol solution was fully evaporated. The same IPLMT process as described above was then applied to generate the functional Zn pattern on the seashell.

Testing of the temperature/humidity sensor, electrodes for measuring electrophysiological signals, and the dipole antenna The sensors were first connected to conductive copper traces through the conductive silver paste. Calibration and testing of the temperature sensor and humidity sensor were achieved by connecting the copper traces to a digital multimeter (Keithley 2401) through alligator clips. Data acquisition software (I-V software) acquired the resistance values from the digital multimeter and recorded them in computers. The electrophysiological signals (e.g., ECG or EMG) were acquired from the electrodes by a commercial biological data acquisition system (Bioamp, ADInstruments). All experiments on human subjects were carried out under the approval of the Institutional Review Board (IRB) at the Pennsylvania State University (protocol numbers: STUDY00008003 and STUDY00009245). The S-parameters (e.g., return losses S<sub>11</sub>) of the antenna were measured by a vector network analyzer (Keysight E5071C) and the resonance frequency of the dipole antenna was determined from the S<sub>11</sub> curve.

# **CRediT authorship contribution statement**

Ning Yi: Conceptualization, Methodology, Validation, Writing - original draft, Writing - review & editing, Visualization. Yuyan Gao: Conceptualization, Methodology, Validation, Writing - review & editing, Visualization. Antonino Lo Verso: Methodology, Writing - original draft, Writing - review & editing. Jia Zhu: Methodology. Daniel Erdely: Methodology. Cuili Xue: Methodology. Robert Lavelle: Methodology. Huanyu Cheng: Conceptualization, Writing - original draft, Writing - review & editing, Visualization, Supervision, Project administration, Funding acquisition.

#### **Declaration of Competing Interest**

The authors declare that they have no known competing financial interests or personal relationships that could have appeared to influence the work reported in this paper.

# Acknowledgments

The manuscript is written through the contributions of all authors. All authors have approved the final version of this manuscript. This research is supported by National Science Foundation (Grant No. ECCS-1933072), the National Heart, Lung, And Blood Institute of the National Institutes of Health under Award Number R61HL154215, and Penn State University. The partial support from the Center for Biodevices, the College of Engineering, the Institute for Computational and Data Sciences, and the Center for Security Research and Education, is also

acknowledged. One or more provisional patents are being filed on this work.

# Appendix A. Supplementary data

Supplementary data to this article can be found online at https://doi.org/10.1016/j.mattod.2021.07.002.

#### References

- [1] S.-W. Hwang et al., Nano Lett. 15 (5) (2015) 2801.
- [2] Y.K. Lee et al., Adv. Mater. 29 (38) (2017) 1702665.
- [3] J. Zimmermann et al., Adv. Funct. Mater. 28 (24) (2018) 1705795.
- [4] K. Sim et al., Nat. Electron. 2 (10) (2019) 471.
- [5] J.J. Adams et al., Adv. Mater. 23 (11) (2011) 1335.
- [6] J.A. Paulsen et al., Printing conformal electronics on 3D structures with Aerosol Jet technology, in: 2012 Future of Instrumentation International Workshop (FIIW) Proceedings, IEEE, 2012, p. 1.
- [7] Z. Zhu et al., Adv. Mater. 30 (23) (2018) 1707495.
- [8] A. Mahajan et al., ACS Appl. Mater. Interfaces 5 (11) (2013) 4856.
- [9] B. Clifford et al., Sens. Actuators, B 255 (2018) 1031.
- [10] B.Y. Ahn et al., Science 323 (5921) (2009) 1590.
- [11] J. Niittynen et al., Sci. Rep. 5 (2015) 8832.
- [12] T. Seifert et al., Ind. Eng. Chem. Res. 54 (2) (2015) 769.
- [13] A.K. Pahari, B.K. Dubey, Waste from electrical and electronics equipment, in: *Plastics to Energy*, Elsevier, 2019, p. 443.
- [14] F. Xu et al., J. Mater. Sci. 53 (4) (2018) 2638.
- [15] X. Huang et al., Adv. Mater. 26 (43) (2014) 7371.
- [16] N. Yi et al., ACS Appl. Mater. Interfaces 10 (43) (2018) 36664.
- [17] S.-K. Kang et al., Nature 530 (7588) (2016) 71.
- [18] G. Lee et al., Adv. Energy Mater. 7 (18) (2017) 1700157.
- [19] H. Tao et al., Proc. Natl. Acad. Sci. 111 (49) (2014) 17385.
- [20] L. Yin et al., Adv. Funct. Mater. 24 (5) (2014) 645.
- [21] B.K. Mahajan et al., Small 13 (17) (2017) 1700065.
- [22] W. Shou et al., Adv. Mater. 29 (26) (2017) 1700172.
- [23] D. Angmo et al., Adv. Energy Mater. 3 (2) (2013) 172.
- [24] M. Hösel, F.C. Krebs, J. Mater. Chem. 22 (31) (2012) 15683.
- [25] Y. Lu, J. Cecil, Int. J. Adv. Manuf. Technol. 84 (5–8) (2016) 1141.
- [26] H. Sundmaeker et al., Cluster of European Research Projects on the Internet of Things, European Commission 3 (3) (2010) 34.
- [27] L. Yan et al., The Internet of things: from RFID to the next-generation pervasive networked systems, Crc Press (2008).
- [28] R. Buyya et al., Future Gener. Comput. Syst. 25 (6) (2009) 599.
- [29] K.M. Koczkur et al., Dalton Trans. 44 (41) (2015) 17883.
- [30] J. Perelaer et al., Adv. Mater. 24 (19) (2012) 2620.
- [31] M. Helgesen et al., Polym. Chem. 3 (9) (2012) 2649.
- [32] A. Yadav et al., Bull. Mater. Sci. 29 (6) (2006) 641.
- [33] U. Gaur et al., J. Phys. Chem. Ref. Data 12 (1) (1983) 65.
- [34] A. Yadav, et al., 29 (6) (2006), 641.
- $[35]\ R.\ Saleh,\ et\ al.,\ 130\ (2014)\ 581.$
- [36] J. Agrawal, et al., 12 (10) (2018) 1800241.
- $[37] \ \ G. \ Seniutinas, \ et \ al., \ 1 \ (2) \ (2016) \ 021301.$
- [38] S.A. Patil, et al., 7 (11) (2017) 6565.
- [39] S. Shariffudin et al., Trans. Electr. Electron. Mater. 13 (2) (2012) 102.
- [40] S.K. Kang et al., Adv. Funct. Mater. 24 (28) (2014) 4427.
- [41] E. Marin et al., Int. J. Nanomed. 8 (2013) 3071.
- [42] A. Ammala, Int. J. Cosmet. Sci. 35 (2) (2013) 113.
- [43] C. Vaida et al., Macromol. Biosci. 10 (8) (2010) 925.
- [44] S.W. Hwang et al., Adv. Mater. 26 (23) (2014) 3905.
- [45] W. Luo et al., J. Phys. Chem. C 112 (7) (2008) 2359.
- [46] O.A. Yeshchenko et al., Phys. Rev. B 75 (8) (2007) 085434.
- [47] S. Ding et al., ACS Appl. Mater. Interfaces 8 (9) (2016) 6190.
- [48] J. Jiu et al., J. Mater. Chem. 22 (44) (2012) 23561.
- [49] J. Fang et al., Cryst. Growth Des. 7 (5) (2007) 864.
- [50] H.-J. Hwang et al., Sci. Rep. 6 (1) (2016) 1.
- [51] M.A. Daniele et al., Adv. Mater. 27 (9) (2015) 1600.
- [52] T.T.S. Lew et al., Adv. Mater. Technol. 5 (3) (2020) 1900657.
- [53] E. Sipilä et al., Int. J. Antenn. Propag. (2016) 2016.
- [54] T. Wang et al., J. Electron. Mater. 36 (10) (2007) 1333.
- [55] L. Yang et al., J. Mater. Chem. A 8 (14) (2020) 6487.
- [56] N. Yi, M. Today, et al., Physics (2020).